International Tables for Crystallography (2006). Vol. C, Section 4.3.8.1, pp. 419–421.

Large gaps at the dispersion surface are associated with strong inner reflections – and a strong dynamical effect of two-beam-like character. The absolute magnitude of the gap – or its inverse, the extinction distance – can be obtained in different ways. Early measurements were based on the split of diffraction spots from a wedge, see Lehmpfuhl (1974), or the corresponding fringe periods measured in bright- and dark-field micrographs (Ando, Ichimiya & Uyeda, 1974). The most precise and applicable large-gap methods are based on the refinement of the fringe pattern in CBED discs from strong reflections, as developed by Goodman & Lehmpfuhl (1967) and Voss, Lehmpfuhl & Smith (1980). In recent years, this technique has been developed to high perfection by means of filtered CBED patterns, see Spence & Zuo (1992) and papers referred to therein. See also Chapter 8.8.

The gap at the dispersion surface can also be obtained directly from the split observed at the crossing of a weak Kikuchi line with a strong band. Gjønnes & Høier (1971) showed how this can be used to determine strong low-order reflections. High voltage may improve the accuracy (Terasaki, Watanabe & Gjønnes, 1979). The sensitivity of the intersecting Kikuchi-line (IKL) method was further increased by the use of CBED instead of Kikuchi patterns (Matsuhata, Tomokiyo, Watanabe & Eguchi, 1984; Taftø & Gjønnes, 1985). In a recent development, Høier, Bakken, Marthinsen & Holmestad (1993) have measured the intensity distribution in the CBED discs around such intersections and have refined the main structure factors involved.

Two-dimensional rocking curves collected by CBED patterns around the axis of a dense zone are complicated by extensive many-beam dynamical interactions. The Bristol–Bath group (Saunders, Bird, Midgley & Vincent, 1994) claim that the strong dynamic effects can be exploited to yield high sensitivity in refinement of low-order structure factors. They have also developed procedures for *ab initio* structure determination based on zone-axis patterns (Bird & Saunders, 1992), see Chapter 8.8.

Determination of phase invariants. It has been known for some time (*e.g* Kambe, 1957) that the dynamical three-beam case contains information about phase. As in the X-ray case, measurement of dynamical effects can be used to determine the value of triplets (Zuo, Høier & Spence, 1989) and to determine phase angles to better than one tenth of a degree (Zuo, Spence, Downs & Mayer, 1993) which is far better than any X-ray method. Bird (1990) has pointed out that the phase of the absorption potential may differ from the phase of the real potential.

Thickness is an important parameter in electron-diffraction experiments. In structure-factor determination based on CBED patterns, thickness is often included in the refinement. Thickness can also be determined directly from profiles connected with large gaps at the dispersion surface (Goodman & Lehmpfuhl, 1967; Blake, Jostsons, Kelly & Napier, 1978; Glazer, Ramesh, Hilton & Sarikaya, 1985). The method is based on the outer part of the fringe profile, which is not so sensitive to the structure factor. The intensity minimum of the ith fringe in the diffracted disc occurs at a position corresponding to the excitation error s_i and expressed as

$$(s_i^2 + 1/\varepsilon_g^2)t^2 = n_i^2, \qquad (4.3.7.9)$$

where n_i is a small integer describing the order of the minimum. This equation can be arranged in two ways for graphic determination of thickness. The commonest method appears to be to plot $(s_i/n_i)^2$ against $1/n_i{}^2$ and then determine the thickness from the intersection with the ordinate axis (Kelly, Jostsons, Blake & Napier, 1975). Glazer *et al.* (1985) claim that the method originally proposed by Ackermann (1948), where s_i^2 is plotted against n_i and the thickness is taken from the slope, is more accurate. In both cases, the outer part of the rocking curve is emphasized; exact knowledge of the gap is not necessary for a good determination of thickness, provided the assumption of a two-beam-like rocking curve is valid.

4.3.8. Crystal structure determination by high-resolution electron microscopy

(By J. C. H. Spence and J. M. Cowley)

4.3.8.1. *Introduction*

For the crystallographic study of real materials, high-resolution electron microscopy (HREM) can provide a great deal of information that is complementary to that obtainable by X-ray and neutron diffraction methods. In contrast to the statistically averaged information that these other methods provide, the great power of HREM lies in its ability to elucidate the detailed atomic arrangements of individual defects and the microcrystalline structure in real crystals. The defects and inhomogeneities of real crystals frequently exert a controlling influence on phase-transition mechanisms and more generally on all the electrical, mechanical, and thermal properties of solids. The real-space images that HREM provides (such as that shown in Fig. 4.3.8.1) can give an immediate and dramatic impression of chemical crystallography processes, unobtainable by other methods. Their atomic structure is of the utmost importance for

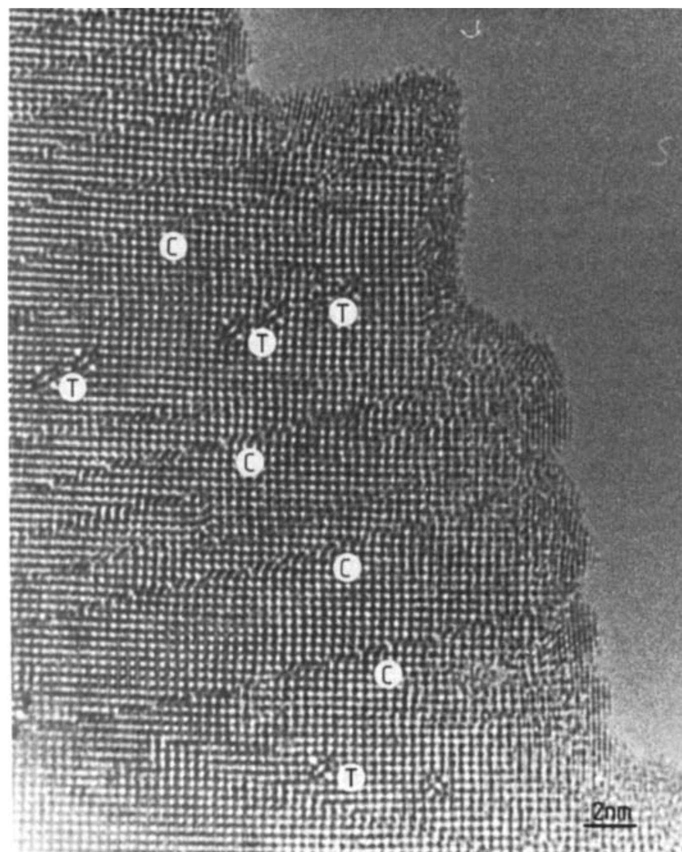

Fig. 4.3.8.1. Atomic resolution image of a tantalum-doped tungsten trioxide crystal (pseudo-cubic structure) showing extended crystallographic shear-plane defects (C), pentagonal-column hexagonal-tunnel (PCHT) defects (T), and metallization of the surface due to oxygen desorption (JEOL 4000EX, crystal thickness less than 200 Å, 400 kV, $C_s = 1$ mm). Atomic columns are black. [Smith, Bursill & Wood (1985).]

Copyright © 2006 International Union of Crystallography

an understanding of the properties of real materials. The HREM method has proven powerful for the determination of the structure of such defects and of the submicrometre-sized microcrystals that constitute many polyphase materials.

In summary, HREM should be considered the technique of choice where a knowledge of microcrystal size, shape or morphology is required. In addition, it can be used to reveal the presence of line and planar defects, inclusions, grain boundaries and phase boundaries, and, in favourable cases, to determine atomic structure. Surface atomic structure and reconstruction have also been studied by HREM. However, meaningful results in this field require accurately controlled ultra-high-vacuum conditions. The determination of the atomic structure of point defects by HREM so far has proven extremely difficult, but this situation is likely to change in the near future.

The following sections are not intended to review the applications of HREM, but rather to provide a summary of the main theoretical results of proven usefulness in the field, a selected bibliography, and recommendations for good experimental practice. At the time of writing (1997), the point resolution of HREM machines lies between 1 and 2 Å.

The function of the objective lens in an electron microscope is to perform a Fourier synthesis of the Bragg-diffracted electron beams scattered (in transmission) by a thin crystal, in order to produce a real-space electron image in the plane r. This electron image intensity can be written

$$|\psi(\mathbf{r})|^2 = \left| \int \Psi(\mathbf{u}) \exp\{2\pi i \mathbf{u} \cdot \mathbf{r}\} P(\mathbf{u}) \exp\{i\chi(\mathbf{u})\} \, \mathrm{d}\mathbf{u} \right|^2, \quad (4.3.8.1)$$

where $\Psi(\mathbf{u})$ represents the complex amplitude of the diffracted wave after diffraction in the crystal as a function of the reciprocal-lattice vector $\mathbf{u}$ [magnitude $(2 \sin\theta)/\lambda$] in the plane perpendicular to the beam, so that the wavevector of an incident plane wave is written $\mathbf{K}_0 = \mathbf{k}_z + 2\pi\mathbf{u}$. Following the convention of Section 2.5.1 in *IT* B (1992), we write $|\mathbf{K}_0| = 2\pi\lambda^{-1}$. The function $\chi(\mathbf{u})$ is the phase factor for the objective-lens transfer function and $P(\mathbf{u})$ describes the effect of the objective aperture:

$$P(\mathbf{u}) = \begin{cases} 1 & \text{for } |\mathbf{u}| < u_0 \\ 0 & \text{for } |\mathbf{u}| \geq u_0. \end{cases}$$

For a periodic object, the image wavefunction is given by summing the contributions from the set of reciprocal-lattice points, $\mathbf{g}$, so that

$$|\psi(\mathbf{r})|^2 = \left| \sum_{\mathbf{g}} \Psi_{\mathbf{g}} \exp\{2\pi i \mathbf{g} \cdot \mathbf{r}\} P(\mathbf{g}) \exp\{i\chi(\mathbf{g})\} \right|^2. \quad (4.3.8.2)$$

For atomic resolution, with $u_0 \approx 1\text{Å}^{-1}$, it is apparent that, for all but the simplest structures and smallest unit cells, this synthesis will involve many hundreds of Bragg beams. A scattering calculation must involve an even larger number of beams than those that contribute resolvable detail to the image, since, as described in Section 2.5.1 in *IT* B (1992), all beams interact strongly through multiple coherent scattering. The theoretical basis for HREM image interpretation is therefore the dynamical theory of electron diffraction in the transmission (or Laue) geometry [see Chapter 5.2 in *IT* B (1992)]. The resolution of HREM images is limited by the aberrations of the objective electron lens (notably spherical aberration) and by electronic instabilities. An intuitive understanding of the complicated effect of these factors on image formation from multiply scattered Bragg beams is generally not possible. To provide a basis for understanding, therefore, the following section treats the simplified case of few-beam 'lattice-fringe' images, in order to expose the relationship between the crystal potential, its structure factors, electron-lens aberrations, and the electron image.

Image formation in the transmission electron microscope is conventionally treated by analogy with the Abbe theory of coherent optical imaging. The overall process is subdivided as follows. (*a*) The problem of beam–specimen interaction for a collimated kilovolt electron beam traversing a thin parallel-sided slab of crystal in a given orientation. The solution to this problem gives the elastically scattered dynamical electron wavefunction $\psi(\mathbf{r})$, where $\mathbf{r}$ is a two-dimensional vector lying in the downstream surface of the slab. Computer algorithms for dynamical scattering are described in Section 4.3.6. (*b*) The effects of the objective lens are incorporated by multiplying the Fourier transform of $\psi(\mathbf{r})$ by a function $T(\mathbf{u})$, which describes both the wavefront aberration of the lens and the diffraction-limiting effects of any apertures. The dominant aberrations are spherical aberration, astigmatism, and defect of focus. The image intensity is then formed from the modulus squared of the Fourier transform of this product. (*c*) All partial coherence effects may be incorporated by repeating this procedure for each of the component energies and directions that make up the illumination from an extended electron source, and summing the resulting intensities. Because this procedure requires a separate dynamical calculation for each component direction of the incident beam, a number of useful approximations of restricted validity have been developed; these are described in Subsection 4.3.8.4. This treatment of partial coherence assumes that a perfectly incoherent effective source can be identified. For field-emission HREM instruments, a coherent sum (over directions) of complex image wavefunctions may be required.

General treatments of the subject of HREM can be found in the texts by Cowley (1981) and Spence (1988). The sign

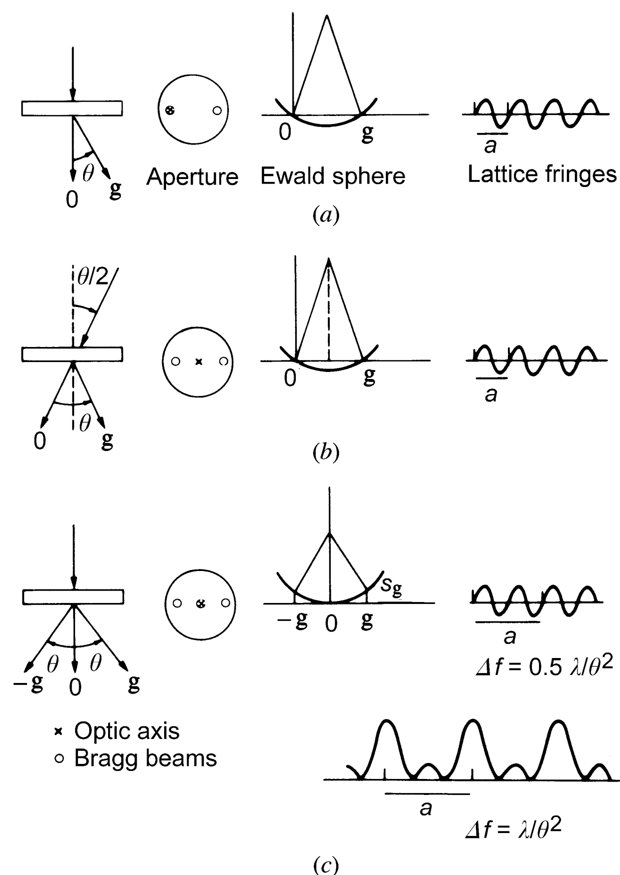

Fig. 4.3.8.2. Imaging conditions for few-beam lattice images. For three-beam axial imaging shown in (*c*), the formation of half-period fringes is also shown.

conventions used throughout the following are consistent with the standard crystallographic convention of Section 2.5.1 of *IT* B (1992), which assumes a plane wave of form $\exp\{-i(\mathbf{k}\cdot\mathbf{r}-\omega t)\}$ and so is consistent with X-ray usage.

4.3.8.2. *Lattice-fringe images*

We consider few-beam lattice images, in order to understand the effects of instrumental factors on electron images, and to expose the conditions under which they faithfully represent the scattering object. The case of two-beam lattice images is instructive and contains, in simplified form, most of the features seen in more complicated many-beam images. These fringes were first observed by Menter (1956) and further studied in the pioneering work of Komoda (1964) and others [see Spence (1988) for references to early work]. The electron-microscope optic-axis orientation, the electron beam, and the crystal setting are indicated in Fig. 4.3.8.2. If an objective aperture is used that excludes all but the two beams shown from contributing to the image, equation (4.3.8.2) gives the image intensity along direction $\mathbf{g}$ for a centrosymmetric crystal of thickness t as

$$\begin{aligned}I(x,t)&=|\Psi_0(t)|^2+|\Psi_{\rm g}(t)|^2\\&\quad+2|\Psi_0||\Psi_{\rm g}|\cos\{2\pi x/d_{\rm g}+\chi(u_{\rm g})\eta_{\rm g}(t)-\eta_0(t)\}.\quad(4.3.8.3)\end{aligned}$$

The Bragg-diffracted beams have complex amplitudes $\Psi_{\rm g}(t)=|\Psi_{\rm g}(t)|\exp\{i\eta_{\rm g}(t)\}$. The lattice-plane period is $d_{\rm g}$ in direction $\mathbf{g}$ [Miller indices (hkl)]. The lens-aberration phase function, including only the effects of defocus Δf and spherical aberration (coefficient C_s), is given by

$$\chi(u_{\rm g})=(2\pi/\lambda)\{(\Delta f\lambda^2u_{\rm g}^2/2)+C_s\lambda^4u_{\rm g}^4/4\}.\qquad(4.3.8.4)$$

The effects of astigmatism and higher-order aberrations have been ignored. The defocus, Δf, is negative for the objective lens weakened (*i.e.* the focal length increased, giving a bright first Fresnel-edge fringe). The magnitude of the reciprocal-lattice vector $u_g=d_g^{-1}=(2\sin\theta_B)/\lambda$, where θ_B is the Bragg angle. If these two Bragg beams were the only beams excited in the crystal (a poor approximation for quantitative work), their amplitudes would be given by the 'two-beam' dynamical theory of electron diffraction as

$$\begin{aligned}\Psi_0(t)&=\{\cos[\pi t(1+w^2)^{1/2}/\xi_{\rm g}]+iw(1+w^2)^{-1/2}\\&\quad\times\sin[\pi t(1+w^2)^{1/2}/\xi_{\rm g}]\}\exp(-i\pi s_{\rm g}t)\\\Psi_{\rm g}(t)&=i(1+w^2)^{-1/2}\sin[\pi t(1+w^2)^{1/2}/\xi_{\rm g}]\\&\quad\times\exp(-\pi is_{\rm g}t),\qquad(4.3.8.5)\end{aligned}$$

where $\xi_{\rm g}$ is the two-beam extinction distance, $V_{\rm g}=\pi/(\sigma\xi_{\rm g})$ is a Fourier coefficient of crystal potential, $s_{\rm g}$ is the excitation error (see Fig. 4.3.8.2), $w=s_{\rm g}\xi_{\rm g}$, and the interaction parameter σ is defined in Section 2.5.1 of *IT* B (1992).

The two-beam image intensity given by equation (4.3.8.3) therefore depends on the parameters of crystal thickness (t), orientation ($s_{\rm g}$), structure factor ($V_{\rm g}$), objective-lens defocus Δf, and spherical-aberration constant C_s. We consider first the variation of lattice fringes with crystal thickness in the two-beam approximation (Cowley, 1959; Hashimoto, Mannami & Naiki, 1961). At the exact Bragg condition ($s_{\rm g}=0$), equations (4.3.8.5) and (4.3.8.3) give

$$I(x,t)=1-\sin(2\pi t/\xi_{\rm g})\sin[2\pi x/d+\chi(u_{\rm g})].\qquad(4.3.8.6)$$

If we consider a wedge-shaped crystal with the electron beam approximately normal to the wedge surface and edge, and take x and $\mathbf{g}$ parallel to the edge, this equation shows that sinusoidal lattice fringes are expected whose contrast falls to zero (and reverses sign) at thicknesses of $t_n=n\xi_{\rm g}/2$. This apparent abrupt translation of fringes (by $d/2$ in the direction x) at particular thicknesses is also seen in some experimental many-beam images. The effect of changes in focus (due perhaps to variations in lens current) is seen to result in a translation of the fringes (in direction x), while time-dependent variations in the accelerating voltage have a similar effect. Hence, time-dependent variations of the lens focal length or the accelerating voltage result in reduced image contrast (see below). If the illumination makes a small angle $\alpha=\lambda u'$ with the optic axis, the intensity becomes

$$\begin{aligned}I(x,\alpha)&=|\Psi_0|^2+|\Psi_{\rm g}|^2+2|\Psi_{\rm g}||\Psi_0|\\&\quad\times\cos[\chi(-u_{\rm g}-u')-\chi(u')+2\pi x/d+\eta_{\rm g}(t)-\eta_0(t)].\end{aligned}$$

For a uniformly intense line source subtending a semiangle θ_c, the total lattice-fringe intensity is

$$I(x)=(1/\theta_c)\textstyle\int I(x,\alpha)\,{\rm d}\alpha.$$

The resulting fringe visibility $C=(I_{\max}-I_{\min})/(I_{\max}+I_{\min})$ is proportional to $C=(\sin\beta)/\beta$, where $\beta=2\pi\Delta f\theta_c/d$. The contrast falls to zero for $\beta=\pi$, so that the range of focus over which fringes are expected is $\Delta z=d/\theta_c$. This is the approximate depth of field for lattice images due to the effects of the finite source size alone.

The case of three-beam fringes in the axial orientation is of more practical importance [see Fig. 4.3.8.2(*b*)]. The image intensity for $\Psi_{\rm g}=\Psi_{-\rm g}$ and $s_{\rm g}=s_{-\rm g}$ is

$$\begin{aligned}I(x,t)&=|\Psi_0|^2+2|\Psi_{\rm g}|^2+2|\Psi_{\rm g}|^2\cos(4\pi x/d)\\&\quad+4|\Psi_0||\Psi_{\rm g}|\cos(2\pi x/d)\\&\quad\times\cos[\chi(u_{\rm g})+\eta_{\rm g}(t)-\eta_0(t)].\qquad(4.3.8.7)\end{aligned}$$

The lattice image is seen to consist of a constant background plus cosine fringes with the lattice spacing, together with cosine fringes of half this spacing. The contribution of the half-spacing fringes is independent of instrumental parameters (and therefore of electronic instabilities if $\theta_c=0$). These fringes constitute an important HREM image artifact. For kinematic scattering, $\eta_{\rm g}(t)-\eta_0(t)=-\pi/2$ and only the half-period fringes will then be seen if $\chi(u_{\rm g})=n\pi$, or for focus settings

$$\Delta f=n\lambda^{-1}u_{\rm g}^{-2}-C_s\lambda^2u_{\rm g}^2/2.\qquad(4.3.8.8)$$

Fig. 4.3.8.2(*c*) indicates the form of the fringes expected for two focus settings with differing half-period contributions. As in the case of two-beam fringes, dynamical scattering may cause Ψ_0 to be severely attenuated at certain thicknesses, resulting also in a strong half-period contribution to the image.

Changes of 2π in $\chi(u_{\rm g})$ in equation (4.3.8.7) leave $I(x,t)$ unchanged. Thus, changes of defocus by amounts

$$\Delta f_f=2n/(\lambda u_{\rm g}^2)\qquad(4.3.8.9)$$

or changes in C_s by

$$\Delta C_s=4n/(\lambda^3u_{\rm g}^4)\qquad(4.3.8.10)$$

yield identical images. The images are thus periodic in both Δf and C_s. This is a restricted example of the more general phenomenon of n-beam Fourier imaging discussed in Subsection 4.3.8.3.

We note that only a single Fourier period will be seen if Δf_f is less than the depth of field Δz. This leads to the approximate condition $\Theta_c>\lambda/d$, which, when combined with the Bragg law, indicates that a single period only of images will be seen when adjacent diffraction discs just overlap.

references